Acta Cryst. (1999). A**55**, 828–839

The phase transitions and crystal structures of $Ba_3RM_2O_{7.5}$ complex oxides (R = rare-earth elements, M = Al, Ga)

A. M. Abakumov,[a,b] R. V. Shpanchenko,[a] O. I. Lebedev,[b]† G. Van Tendeloo,[b]* S. Amelinckx[b] and E. V. Antipov[a]

[a]*Department of Chemistry, Moscow State University, Moscow 119899, Russia, and* [b]*EMAT, University of Antwerp (RUCA), Groenenborgerlaan 171, B-2020 Antwerp, Belgium. E-mail: gvt@ruca.ua.ac.be*

(*Received 16 October 1998; accepted 1 February 1999*)

Abstract

The structures of α-$Ba_3RAl_2O_{7.5}$ and β-$Ba_3RM_2O_{7.5}$ complex oxides (R = rare-earth elements, M = Al, Ga) have been studied by a combination of X-ray diffraction, electron diffraction (ED) and high-resolution electron microscopy (HREM). The α and β forms have cell parameters related to the perovskite subcell: $a = 2a_{per}$, $b = a_{per}(2)^{1/2}$, $c = 3a_{per}(2)^{1/2}$, however, the α form has an orthorhombic unit cell whereas the β form adopts monoclinic symmetry. The crystal structure of monoclinic $Ba_3ErGa_2O_{7.5}$ was refined from X-ray powder data (space group $P2/c$, a = 7.93617 (9), b = 5.96390 (7), c = 18.4416 (2) Å, β = 91.325 (1)°, R_I = 0.023, R_P = 0.053), the structure of the α form (space group $Cmc2_1$) was deduced from ED and HREM data. The important feature of the α and β structures is the presence of slabs containing strings of vertex-sharing tetrahedral Al_2O_7 pairs. Two almost equivalent oxygen positions within the strings can be occupied either in an ordered manner leading to the low-temperature β phase or randomly resulting in the high-temperature α structure. The critical temperature of this order–disorder phase transition was determined by high-temperature X-ray diffraction and by differential thermal analysis (DTA). *In situ* ED and HREM observations of the second-order phase transition confirmed the symmetry changes and revealed numerous defects (twins and antiphase boundaries) formed during the phase transformation.

1. Introduction

The complex oxides with common composition $A_3BB'_2O_{7.5}$ [A alkaline-earth cations (Ba, Sr, Ca), B rare-earth elements (Y, Sc), B' small trivalent transition-metal cations (Al^{3+}, Ga^{3+}, Fe^{3+})] show a large variety of crystal structures owing to the possibilities of ordering between B and B' cations with significantly different sizes and the formation of either octahedral or tetrahedral oxygen coordination around B' cations. For large rare-earth cations (La, Nd), the $Ba_6Nd_2Al_4O_{15}$ = 2 × $Ba_3NdAl_2O_{7.5}$ structural type was studied (Mevs & Müller-Bushbaum, 1990; Rüter & Müller-Bushbaum, 1989*a*, 1990*a*,*b*,*c*). This compound has a hexagonal unit cell where Ba and Nd statistically occupy one of the A sites whilst Al cations are distributed between tetrahedral and octahedral interstices in the Ba/O framework. A decrease of the ionic radius of the rare-earth cations leads to an ordered orthorhombic $Ba_6Dy_2Al_4O_{15}$ structure, which contains a framework of Al_2O_7 groups (two AlO_4 tetrahedra with common vertex) connected by corner sharing to DyO_6 octahedra (Rüter & Müller-Bushbaum, 1989*b*).

Formally, the phases with $A_3BB'_2O_{7.5}$ (ABO_{3-x}) composition could be considered as perovskite-related anion-deficient compounds. However, both structures described above cannot be derived from the perovskite structure and must be considered as two individual structural types. The investigation of the BaO–R_2O_3–Al_2O_3 system at 1470 K revealed the formation of the anion-deficient perovskite-like phases $Ba_3RAl_2O_{7.5}$ (R = Nd–Lu, Y) (Kovba *et al.*, 1984). These compounds were found in two forms, a high-temperature α phase and a low-temperature β phase. Both forms have cell parameters related to the perovskite subcell: $a = 2a_{per}$, $b = a_{per}(2)^{1/2}$, $c = 3a_{per}(2)^{1/2}$. However, the α form has an orthorhombic unit cell whereas the β form adopts monoclinic symmetry with a monoclinic angle $\beta \simeq 91.5°$. In $Ba_3RGa_2O_{7.5}$ compounds, only the monoclinic form was observed (Kovba *et al.*, 1987) and these compounds do not exhibit a phase transition up to the melting point. At present, the crystal structures of both forms are still unknown. The vibrational spectra of β-$Ba_3RAl_2O_{7.5}$ show the presence of absorption bands in the high-frequency range which are typical for pairs of vertex-sharing AlO_4 tetrahedra (Porotnikov *et al.*, 1991). Perhaps, the α and β modifications differ by a different kind of ordering of oxygen atoms and anion vacancies.

The goal of the present work is to elaborate the crystal structures of the α and β forms by means of X-ray diffraction, electron diffraction and high-resolution electron microscopy and to study *in situ* the $\alpha \leftrightarrow \beta$ phase transition.

† On leave from the Institute of Crystallography, Russian Academy of Science, 117333 Moscow, Russia.

ISSN 0108-7673

Table 1. *Temperatures of the $\alpha \leftrightarrow \beta$ phase transitions for $Ba_3RAl_2O_{7.5}$ compounds with different rare-earth elements*

Composition	$T_{\alpha\leftrightarrow\beta}$ (K)	$r(R^{3+})$ for CN = 6 (Å)
$Ba_3NdAl_2O_{7.5}$	643	0.995
$Ba_3EuAl_2O_{7.5}$	548	0.950
$Ba_3DyAl_2O_{7.5}$	523	0.908
$Ba_3YAl_2O_{7.5}$	508	0.892
$Ba_3ErAl_2O_{7.5}$	498	0.881
$Ba_3LuAl_2O_{7.5}$	448	0.848

2. Experimental

The $Ba_3RM_2O_{7.5}$ (R = Nd, Eu, Dy, Er, Lu, Y, Sc, M = Al, Ga) samples were prepared by a routine ceramic technique. Stoichiometric amounts of $BaCO_3$, R_2O_3, Al_2O_3 or Ga_2O_3 were ground in an agate mortar under acetone and pressed into pellets. The pellets were annealed in alumina crucibles at 1270 K and 1470 K for 150–200 h in air and then furnace cooled.

The X-ray diffraction patterns were obtained using a focusing Guinier camera FR-552 (Cu $K\alpha_1$ radiation, germanium was used as an internal standard). Raw data for powder structure refinement were collected on a Stadi-P diffractometer (Cu $K\alpha_1$ radiation, curved Ge monochromator, transmission mode, step 0.02°2θ, scintillation counter). High-temperature X-ray diffraction experiments were carried out using a Guinier–Lenne chamber (Cu $K\alpha$ radiation).

The crystal structures were calculated with the *CSD* program package (Akselrud *et al.*, 1989). The *RIETAN*-97 (Izumi, 1993) program was used for powder structure refinement. The final refinement was carried out by the Rietveld method with a pseudo-Voigt profile function.

Differential thermal analysis has been performed with PRT-1000M equipment with heating rate 10° min^{-1} and cooling rate 5° min^{-1}.

Electron diffraction (ED) and high-resolution electron-microscopy (HREM) investigations were made on crushed $Ba_3DyAl_2O_{7.5}$ and $Ba_3EuAl_2O_{7.5}$ samples deposited on holey carbon grids. The ED patterns in the temperature region from 298 to 1070 K were obtained in a Philips CM20 equipped with a double-tilt heating holder. The HREM observations were performed using a JEOL 4000 EX microscope operating at 400 kV. The phase transformation was achieved by variation of the intensity of the incident electron beam. Image simulations were carried out with MacTempas software.

3. Results and discussion

3.1. *Sample characterization*

The room-temperature X-ray powder diffraction patterns of $Ba_3RM_2O_{7.5}$ samples were indexed on a monoclinic lattice with cell parameters $a = 2a_{per}$, $b = a_{per}(2)^{1/2}$, $c = 3a_{per}(2)^{1/2}$ and $\beta \simeq 91.2$–$91.6°$ [a = 7.8423 (9), b = 5.9179 (7), c = 18.412 (2) Å, β = 91.298 (9)° for $Ba_3DyAl_2O_{7.5}$]. The values of the cell parameters are in agreement with those previously published (Kovba *et al.*, 1984, 1987). The only exception is the $Ba_3ScGa_2O_{7.5}$ compound, which has an orthorhombic unit cell with parameters a = 18.189 (1), b = 7.8938 (8), c = 5.8303 (5) Å.

Table 1 represents the critical temperatures of the $\alpha \leftrightarrow \beta$ phase transitions determined by high-temperature X-ray diffraction and DTA analysis. The typical X-ray diffraction pattern at different temperatures taken from the $Ba_3NdAl_2O_{7.5}$ sample is shown in Fig. 1. The appearance of the splitting of the strongest 132_o reflection (o stands for orthorhombic) clearly marks the transition temperature of 643 K. The temperature of the phase transition decreases almost linearly with decreasing size of the rare-earth cation. The DTA measurements for several thermal cycles (heating up and cooling down) revealed that the phase transition is reversible and the difference between transition temperatures on heating and on cooling for $Ba_3NdAl_2O_{7.5}$ (the thermal hysteresis) does not exceed 2 K. For $Ba_3LuAl_2O_{7.5}$, the difference is larger, possibly due to the smaller diffusion ability of atoms at lower

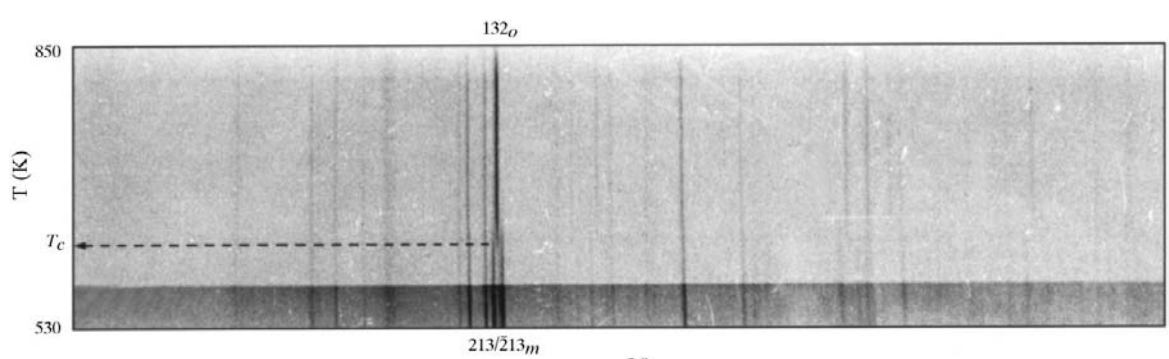

Fig. 1. High-temperature Guinier–Lenné X-ray diffraction pattern of the $Ba_3NdAl_2O_{7.5}$ sample. The temperature of the $\alpha \leftrightarrow \beta$ phase transitions is indicated by the splitting of the strongest 132_o reflection.

temperature. The low values of the transition temperatures suggest no significant rearrangements in the cation sublattice but could be sufficient for the migration of O atoms.

3.2. *Electron diffraction study*

The $[100]^*_m$, $[010]^*_m$ and $[1\bar{1}0]^*_m$ (m refers to the monoclinic unit cell) ED patterns for β-$Ba_3DyAl_2O_{7.5}$ were obtained at room temperature (Fig. 2, left column). The diffraction patterns were completely indexed using the cell parameters determined from X-ray powder diffraction. The angles between rows of $h00$ and $00l$, $hh0$ and $00l$ reflections for $[010]^*_m$ and $[1\bar{1}0]^*_m$, respectively, deviate from 90° indicating a monoclinic distortion with $\beta \simeq 91.3°$. $[010]^*_m$ and $[1\bar{1}0]^*_m$ ED patterns often exhibit splitting of the $h00$ and $hh0$ spots (Fig. 3, left column), which is attributed to twinning. In the $[010]^*_m$ pattern, only $h0l$ reflections with $l = 2n$ are present; this diffraction condition is consistent with the space groups Pc and $P2/c$. However, $00l$ reflections with l odd were found in the $[100]^*_m$ and $[1\bar{1}0]^*_m$ patterns, their intensity is

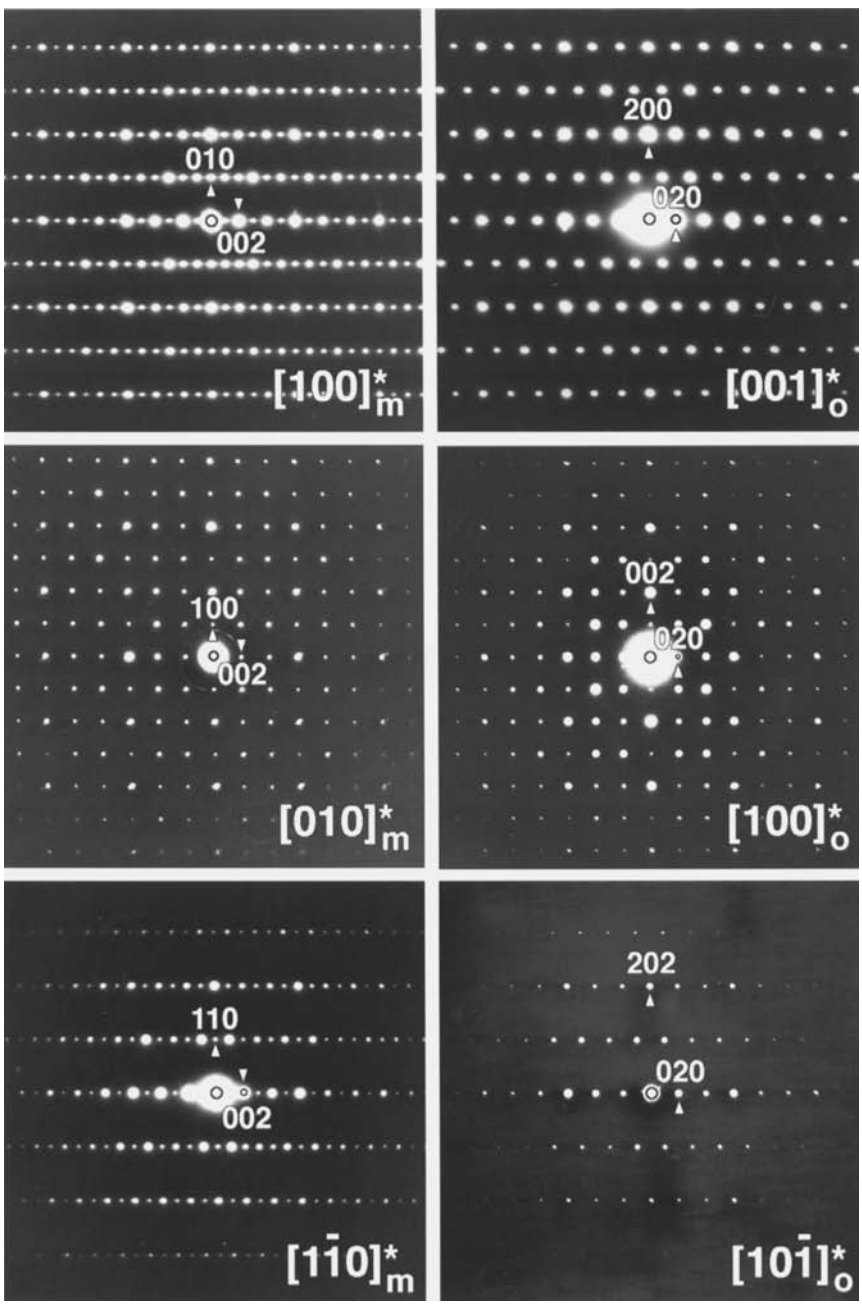

Fig. 2. Electron diffraction patterns along the main zone axes for β-$Ba_3DyAl_2O_{7.5}$ (left column) and α-$Ba_3DyAl_2O_{7.5}$ (right column).

systematically lower than the intensity of the spots with l even. The spots with l odd disappear when the crystallite is tilted around the $00l$ row so as to avoid double-diffraction conditions. Consequently, these spots are attributed to double diffraction and do not violate the suggested diffraction condition.

Heating of the sample introduces significant changes in the electron diffraction patterns. Fig. 3 reproduces the diffraction patterns obtained at 298 K and at 620 K. The ED patterns taken at 298 K from twinned regions of the β phase (left column) exhibit well pronounced splitting of spots which disappears completely when the temperature is increased to 620 K (right column). The transition temperatures determined visually by observing the disappearance of the splitting are 553 K for $Ba_3EuAl_2O_{7.5}$ and 518 K for $Ba_3DyAl_2O_{7.5}$; these values correspond well with the temperatures determined by DTA (Table 1). Heating from 620 K up to 1070 K does not lead to any further changes in the diffraction pattern. When the sample is cooled back to 298 K, the β phase is restored, which confirms the reversibility of the phase transition.

The $[001]^*_m$, $[100]^*_m$ and $[10\bar{1}]^*_m$ ED patterns of the high-temperature α phase obtained at 523 K are shown in the right column of Fig. 2. They exhibit orthorhombic symmetry and are indexed on the basis of the following cell parameters: $a_o = b_m$, $b_o = c_m$ and $c_o = a_m$. All diffraction patterns show the absence of reflections hkl with $h + k \neq 2n$, which indicates the presence of a base-centered unit cell. The weakness of the $00l$, l odd, reflections in the $[100]^*_m$ pattern indicates that their presence is due to double diffraction; it was confirmed by tilting around the $00l$ row. The hkl, $h + k = 2n$, $00l$, $l = 2n$, set of diffraction conditions leads to the possible space group $C222_1$. It should be noted that the observed diffraction conditions are also consistent with the space group $Cmc2_1$. The two groups could be distinguished by observations on the $[010]^*_m$ diffraction pattern where the reflections $h0l$, $l \neq 2n$ should be forbidden in the case of the $Cmc2_1$ space symmetry. However, this zone axis is along the shortest reciprocal-cell vector b^*_o and the possible diffraction from high-order Laue zones prevents an unambiguous determination of the diffraction conditions.

No ED patterns that could be indexed on a hexagonal lattice as described for $Ba_6Nd_2Al_4O_{15}$ (Rüter & Müller-Bushbaum, 1989*a*) or on an orthorhombic lattice like that of $Ba_6Dy_2Al_4O_{15}$ (Rüter & Müller-Bushbaum, 1989*b*) were not observed either at room temperature or at high temperature.

3.3. *Crystal structures of α and β phases*

A single crystal of α-$Ba_3NdAl_2O_{7.5}$ was obtained by melting this compound at 1870 K followed by cooling to 1070 K and quenching in air. The crystal was orthorhombic with cell parameters a_o = 5.9971 (8), b_o = 18.514 (2), c_o = 7.945 (1) Å. Unfortunately, the low quality of the single crystal allows one to build only a rough model of the crystal structure. Nevertheless, the determined atomic coordinates were used to build trial structural models for further investigations.

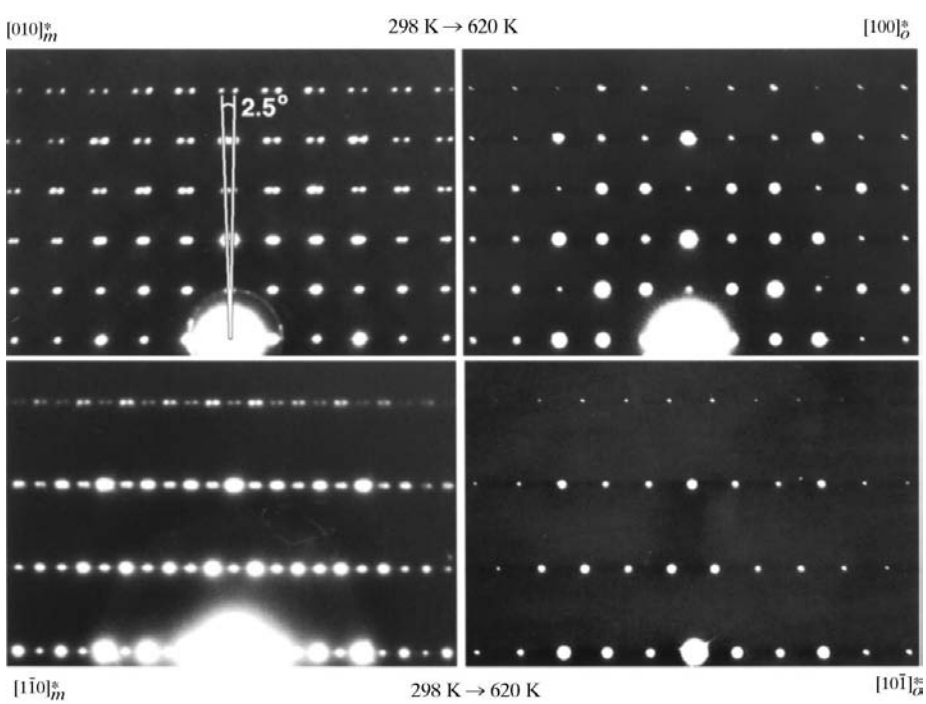

Fig. 3. Changes of the diffraction patterns from twinned regions of monoclinic β-$Ba_3DyAl_2O_{7.5}$ phase upon transition into the orthorhombic α-$Ba_3DyAl_2O_{7.5}$ phase during heating from 298 K (left column) to 623 K (right column).

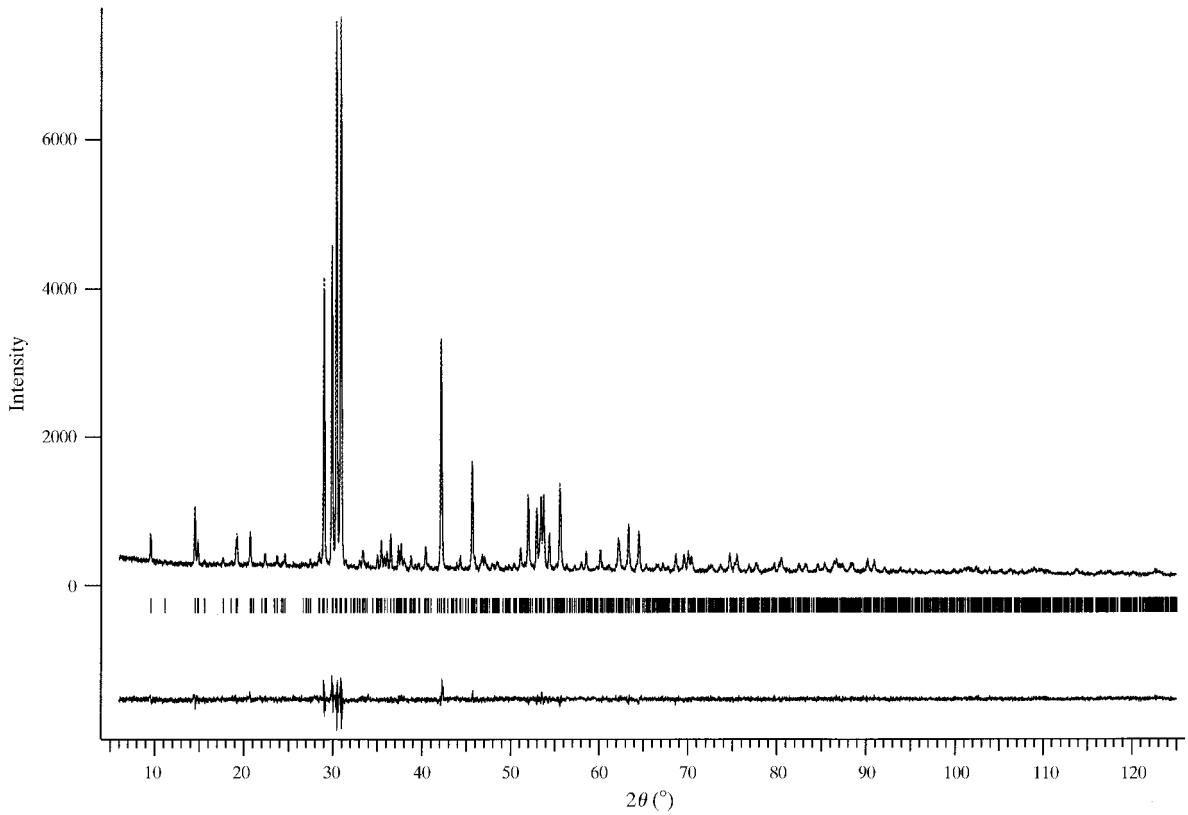

Fig. 4. Experimental, calculated and difference X-ray diffraction patterns for $Ba_3ErGa_2O_{7.5}$.

$Ba_3ErGa_2O_{7.5}$ was chosen for powder refinement of the crystal structure in the monoclinic form. It is known that the Ga-containing compounds do not exhibit the high-temperature orthorhombic form (Kovba *et al.*, 1987). This allows us to avoid a possible intermixing of phases with close cell parameters. The starting atomic coordinates were taken from the model of the α-$Ba_3NdAl_2O_{7.5}$ crystal structure and transformed to the $P2/c$ space group, the most symmetrical one determined from electron diffraction. The thermal parameters for Ba, Ga and O atoms were combined in three separate blocks and refined in an isotropic approximation. After several refinement cycles, good values of reliability factors were obtained: $R_I = 0.023$, $R_P = 0.053$, $R_{wP} = 0.068$. The parameters of the Rietveld refinement are given in Table 2, positional and thermal parameters and selected interatomic distances are listed in Tables 3 and 4. Experimental, calculated and difference X-ray patterns are shown in Fig. 4.†

Two most informative $[100]_m$ and $[010]_m$ projections of the $Ba_3ErGa_2O_{7.5}$ crystal structure (Figs. 5*a*, *b*) show the connection with the perovskite structure. All *A* and *B* cations occupy positions that are close to their positions in perovskite. The placement of Er and Ga in the *B* sublattice is ordered which allows us to divide the structure into two blocks, alternating along $[001]_m$. The first one contains Er and Ga(1) cations ordered on a 'chessboard' pattern. Er has a distorted octahedral oxygen environment; the ErO_6 octahedra are connected with the $Ga(1)O_4$ tetrahedra by vertex sharing *via* two apical O(2), O(3) and two equatorial O(6), O(7) atoms. These Er–Ga(1) blocks have a width of two ErO_6 octahedra edges and they are separated by layers of $Ga(2)O_4$ tetrahedra. These tetrahedra have a common vertex O(1) and form Ga_2O_7 groups; the Ga_2O_7 groups in two Ga(2) layers on both sides of the Er–Ga(1) block are placed on the same level along the a_m axis and shifted over one half of the repeat period along the b_m axis. The alternating Er–Ga(1) blocks and Ga(2) layers are connected together by common atoms O(4) and O(5).

If viewed along the $[010]_m$ direction, the structure can be described as a layer sequence repeated along the *a* axis:

† The numbered intensity of each point on the profile has been deposited with the IUCr. These data are available from the IUCr electronic archives (Reference: SP0165). Services for accessing these data are described at the back of the journal.

Table 2. *Parameters from the Rietveld refinement of the $Ba_3ErGa_2O_{7.5}$ crystal structure*

Space group	$P2/c$
a (Å)	7.93617 (9)
b (Å)	5.96390 (7)
c (Å)	18.4416 (2)
β (°)	91.325 (1)
Z	4
Cell volume (Å^3)	872.62 (2)
Calculated density (g cm^{-3})	6.384
2θ range, step (°)	$5 \le 2\theta \le 125$, 0.02
Number of reflections	1399
Refineable parameters	62
R_I, R_P, R_{wP}	0.023, 0.053, 0.068

–BaO–$Er_{1/3}Ga_{2/3}O_{5/3}\square_{1/3}$–$BaO_{2/3}\square_{1/3}$–$Ga_{2/3}Er_{1/3}O_{5/3}\square_{1/3}$–BaO–

where □ means anion vacancy. This sequence is similar to the perovskite layer sequence along the fourfold axis of a cubic unit cell: –*A*O–*B*O_2–*A*O–. Clearly, all BO_{2-x} layers contain anion vacancies, but only one half of the *A*O layers are anion deficient. The ordering of the Er and Ga(1) cations and the alternation of BaO and $BaO_{2/3}\square_{1/3}$ layers lead to a doubling of the cell parameter $a_m = 2a_{per}$ in comparison with the parameter of the perovskite subcell.

The known cell dimensions and the space symmetry allow one to build a model for the crystal structure of the α phase. The low $\alpha \leftrightarrow \beta$ transition temperature and the close values of the cell parameters for the α and β phases confirm that the phase transformation is not accompanied by a significant rearrangement of the cation sublattice. The atomic coordinates for the β phase were transformed from the monoclinic $P2/c$ unit cell to the orthorhombic $C222_1$ and $Cmc2_1$ unit cells to obtain the structure of the α phase (Figs. 5*c*, *d*). However, both orthorhombic space groups do not contain twofold positions and the O atoms forming a common vertex of the tetrahedra in the Al_2O_7 group should occupy a fourfold position with an occupancy of one half. It means that these O atoms are not placed in the $(x, y, 0)_o$ plane only, but also occupy positions in the $(x, y, 1/2)_o$ plane. They are randomly distributed between two planes resulting in equivalent compositions for barium–

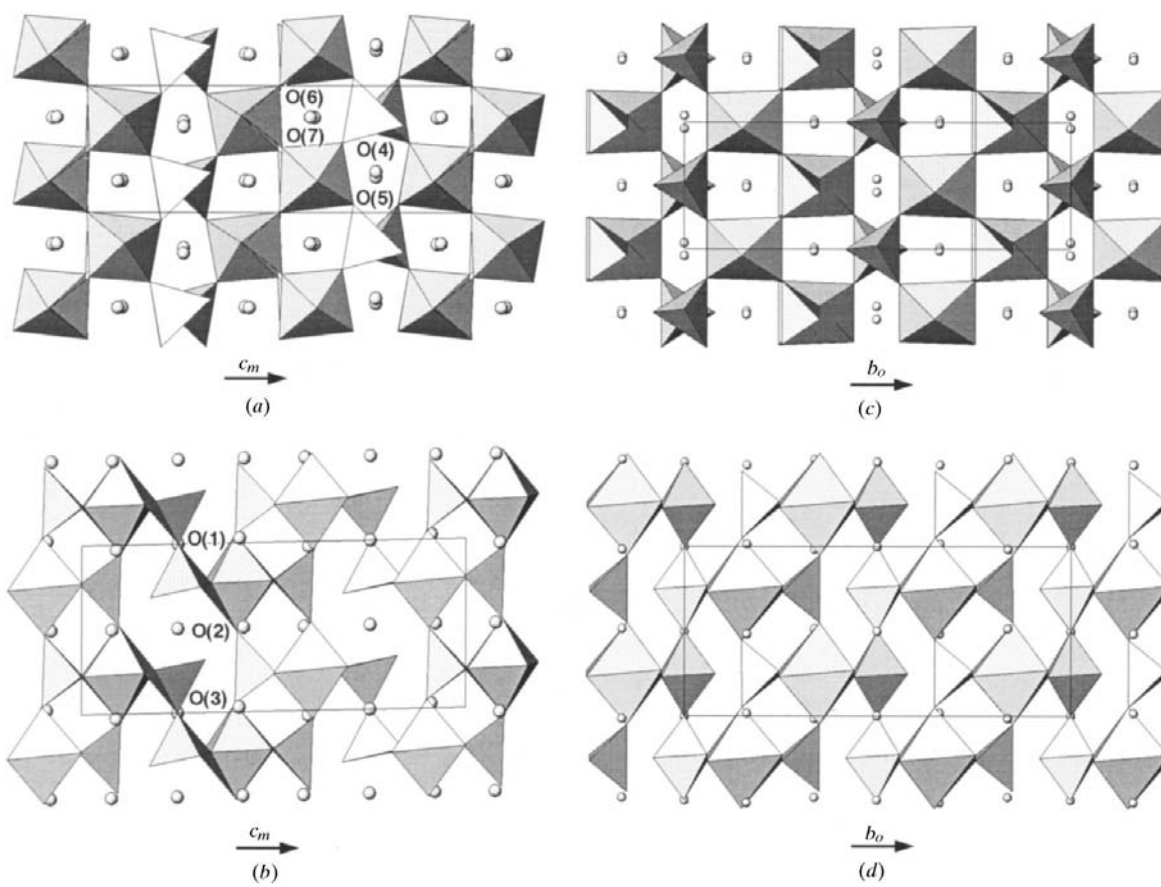

Fig. 5. Projections of the crystal structures of the β phase (left column) along $[100]_m$ (*a*) and $[010]_m$ (*b*) and of the α phase (right column) along $[001]_o$ (*c*) and $[100]_o$ (*d*). Ga(Al) atoms and rare-earth cations are located in tetrahedra and octahedra, respectively. Ba atoms are imaged as shaded spheres.

Table 3. *Positional and thermal parameters for $Ba_3ErGa_2O_{7.5}$*

	Position	x	y	z	B_{iso} (Å^2)
Ba(1)	2(e)	0	0.280 (1)	1/4	0.69 (6)
Ba(2)	2(f)	1/2	0.322 (1)	1/4	0.69 (6)
Ba(3)	4(g)	0.0286 (5)	0.750 (1)	0.0903 (2)	0.69 (6)
Ba(4)	4(g)	0.5001 (5)	0.247 (1)	0.5795 (2)	0.69 (6)
Er	4(g)	0.2470 (6)	0.249 (1)	0.4106 (3)	0.7 (1)
Ga(1)	4(g)	0.248 (1)	0.253 (2)	0.0585 (5)	0.7 (1)
Ga(2)	4(g)	0.232 (1)	0.774 (1)	0.2677 (5)	0.7 (1)
O(1)	2(e)	0	0.785 (9)	1/4	0.7 (3)
O(2)	4(g)	0.044 (4)	0.760 (9)	0.602 (1)	0.7 (3)
O(3)	4(g)	0.473 (4)	0.239 (9)	0.097 (1)	0.7 (3)
O(4)	4(g)	0.267 (5)	0.066 (6)	0.311 (2)	0.7 (3)
O(5)	4(g)	0.249 (5)	0.548 (6)	0.334 (2)	0.7 (3)
O(6)	4(g)	0.232 (7)	0.520 (9)	0.492 (3)	0.7 (3)
O(7)	4(g)	0.231 (7)	−0.003 (9)	0.003 (3)	0.7 (3)
O(8)	4(g)	0.314 (4)	0.319 (5)	0.679 (2)	0.7 (3)

oxygen layers. The orthorhombic structure can be described by the stacking sequence:

$$-BaO_{5/6}\square_{1/6}-R_{1/3}Al_{2/3}O_{5/3}\square_{1/3}-BaO_{5/6}\square_{1/6}-Al_{2/3}R_{1/3}O_{5/3}\square_{1/3}-BaO_{5/6}\square_{1/6}-$$

where now all Ba–O layers are anion deficient.

The structure of the Al(2) layers could also be considered as strings of Al(2) and O(1) atoms. For the α and β phases, the sequences of atoms in these strings are different: –Al(2)–O(1)–Al(2)–□–Al(2)– for the β phase and –Al(2)–$O(1)_{0.5}\square_{0.5}$–Al(2)–$O(1)_{0.5}\square_{0.5}$–Al(2)– for the α phase. The anion positions between two Al(2) atoms have a very similar coordination environment. Taking into account the ionic approximation for the crystal, one can propose that the energies of electrostatic interaction for the two positions are very close and O(1) atoms can easily jump from an occupied into a vacant site. From this point of view, the $\alpha \leftrightarrow \beta$ phase transformation can be attributed to a transition between an ordered and a disordered placement of the O(1) atoms. This order–disorder transition results from a sequential displacement of O atoms along the strings and could be considered as a second-order phase transition where the value of the monoclinic β angle could be chosen as an order parameter. In this case, the Landau–Lifshitz rule imposes a restriction on the relationship between the space symmetry of the high-temperature phase and that of the low-temperature phase. From the two possible monoclinic space groups and the two possible orthorhombic ones, only Pc and $Cmc2_1$ may describe the symmetry of respectively the low-temperature and the high-temperature phases connected by a second-order phase transition since Pc is a subgroup of $Cmc2_1$. It is thus reasonable to assume the Pc symmetry for β-$Ba_3RAl_2O_{7.5}$ and $Cmc2_1$ for α-$Ba_3RAl_2O_{7.5}$. However, this consideration cannot be applied for the Ga-containing compounds since they do not exhibit a phase transition and the space group for the $Ba_3ErGa_2O_{7.5}$ compound is $P2/c$.

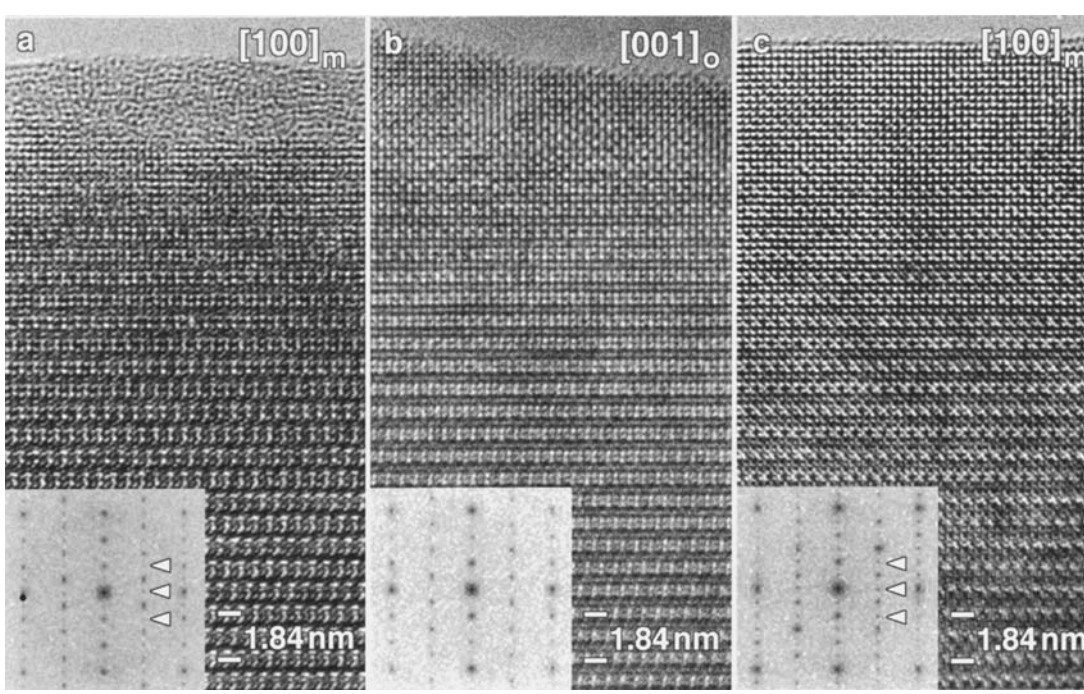

Fig. 6. $[100]_m = [001]_o$ HREM images of one crystallite of $Ba_3DyAl_2O_{7.5}$ showing the transformation from the β (a) into the α phase (b) and back into the β phase (c) by changing the beam intensity. The optical diffraction patterns are shown in the insets. The $hk0$, $h+k\neq 2n$ reflections disappear on the optical diffraction pattern of the α phase due to formation of a C-centered unit cell.

Table 4. *Selected interatomic distances for $Ba_3ErGa_2O_{7.5}$ (Å)*

Ba(1)—O(1)	2.95 (5) × 1	Ba(3)—O(6)	2.88 (6) × 1	Er—O(2)	2.32 (3) × 1
Ba(1)—O(1)	3.01 (5) × 1	Ba(3)—O(6)	2.94 (6) × 1	Er—O(3)	2.23 (3) × 1
Ba(1)—O(2)	2.77 (2) × 2	Ba(3)—O(7)	2.73 (6) × 1	Er—O(4)	2.15 (4) × 1
Ba(1)—O(4)	2.70 (5) × 2	Ba(3)—O(7)	3.05 (6) × 1	Er—O(5)	2.28 (4) × 1
Ba(1)—O(5)	2.95 (4) × 2	Ba(3)—O(8)	2.79 (3) × 1	Er—O(6)	2.21 (6) × 1
Ba(2)—O(3)	2.87 (2) × 2	Ba(4)—O(3)	2.92 (5) × 1	Er—O(7)	2.25 (6) × 1
Ba(2)—O(4)	2.67 (4) × 2	Ba(4)—O(3)	3.09 (5) × 1	Ga(1)—O(2)	1.83 (3) × 1
Ba(2)—O(5)	2.89 (4) × 2	Ba(4)—O(5)	2.80 (4) × 1	Ga(1)—O(3)	1.91 (3) × 1
Ba(2)—O(8)	2.90 (3) × 2	Ba(4)—O(6)	2.88 (6) × 1	Ga(1)—O(6)	1.83 (6) × 1
Ba(3)—O(1)	2.966 (5) × 1	Ba(4)—O(6)	3.10 (6) × 1	Ga(1)—O(7)	1.84 (6) × 1
Ba(3)—O(2)	2.93 (5) × 1	Ba(4)—O(7)	2.92 (6) × 1	Ga(2)—O(1)	1.864 (8) × 1
Ba(3)—O(2)	3.05 (5) × 1	Ba(4)—O(7)	3.04 (6) × 1	Ga(2)—O(4)	1.93 (4) × 1
Ba(3)—O(5)	2.90 (4) × 1	Ba(4)—O(8)	2.42 (4) × 1	Ga(2)—O(5)	1.82 (4) × 1
				Ga(2)—O(8)	1.86 (4) × 1

3.4. *HREM of the perfect structures*

It was found that the local heating produced by a 400 kV electron beam was strong enough to induce the phase transformation; this allows us to observe the $\alpha \leftrightarrow \beta$ phase transition under HREM conditions by changing the intensity of the incident beam. $[100]_m$ = $[001]_o$ HREM images obtained from the same crystallite of $Ba_3DyAl_2O_{7.5}$ at different intensities of the primary electron beam are shown in Fig. 6. The changes in the optical diffraction patterns obtained from the HREM images clearly reveal the phase transformation. Under these particular experimental conditions, the double rows of bright dots correspond to the projection of Dy–Al(1) blocks whereas the single rows of less bright dots image the Al(2) layers. The square array of bright dots spaced by 3 Å which is visible in the thinnest part of the crystallite corresponds to the columns of *A* and *B* cations in the perovskite structure. The images of the monoclinic and the orthorhombic phases look very similar since the projections of both structures along this direction are almost identical (Fig. 5).

The $[010]_m$ = $[100]_o$ projection is more informative since it allows observation of the difference between the α phase and the β phase. The $[010]_m$ image (Fig. 7*a*) shows very bright dots placed at each repeat period along a_m and at half of the repeat period along c_m. According to image simulations, these bright dots correspond to projections of channels in Dy–Al(1) blocks surrounded by Ba(3) atoms. The two types of channels in this block are placed between the Ba(3) and Ba(4) atoms, respectively. They are not symmetrically equivalent owing to the monoclinic distortion and produce a significantly different contrast on the HREM image of the β phase. In contrast to that, the $[100]_o$ image of the α phase (Fig. 7*b*) does not exhibit a well pronounced difference between projections of these channels since their shape becomes identical for the $Cmc2_1$ space symmetry of the α phase. The images calculated for the $[010]_m$ zone of β-$Ba_3DyAl_2O_{7.5}$ (Fig. 8*a*) and the $[100]_o$ zone of α-$Ba_3DyAl_2O_{7.5}$ (Fig. 8*b*) using the crystal structures described above are in agreement with the observed image contrast.

3.5. *Defect structures*

High-resolution images along the $[010]_m$ zone (Fig. 9) reveal the presence of coherent twins in the $(001)_m$ plane of the monoclinic phase. In the diffraction pattern along the same zone (Fig. 3), the twins are revealed by the presence of split spots. A row of unsplit spots is found along the $[001]^*_m$ direction; all other spots are split,

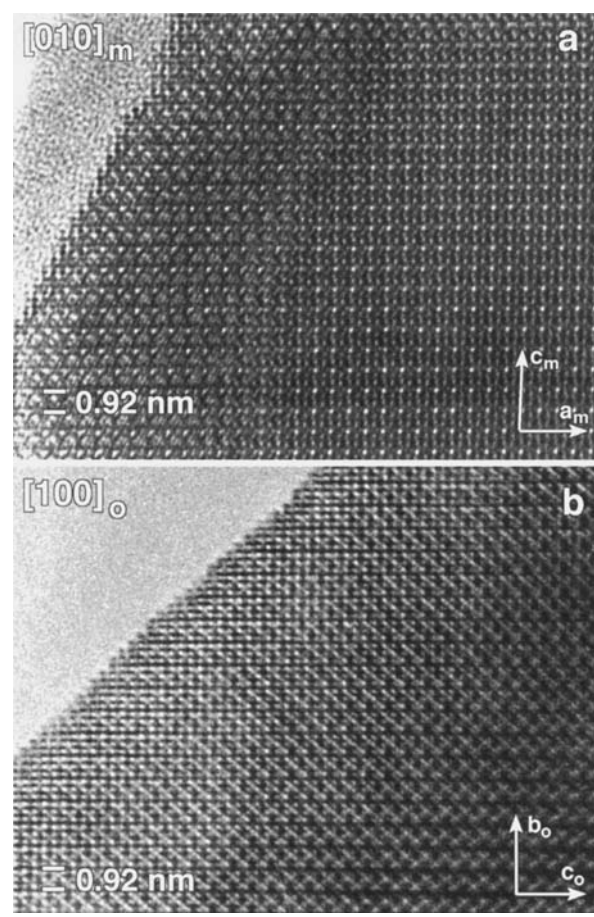

Fig. 7. $[010]_m$ HREM image of β-$Ba_3DyAl_2O_{7.5}$ (*a*) and $[100]_o$ image of α-$Ba_3DyAl_2O_{7.5}$ (*b*).

the direction of splitting is parallel to the unsplit row and the magnitude of the splitting increases linearly with the distance from the unsplit row. These features form the signature of twinning with a coherent twin plane perpendicular to $[001]^*_m$; this is also in accordance with the high-resolution images. The angle enclosed by the

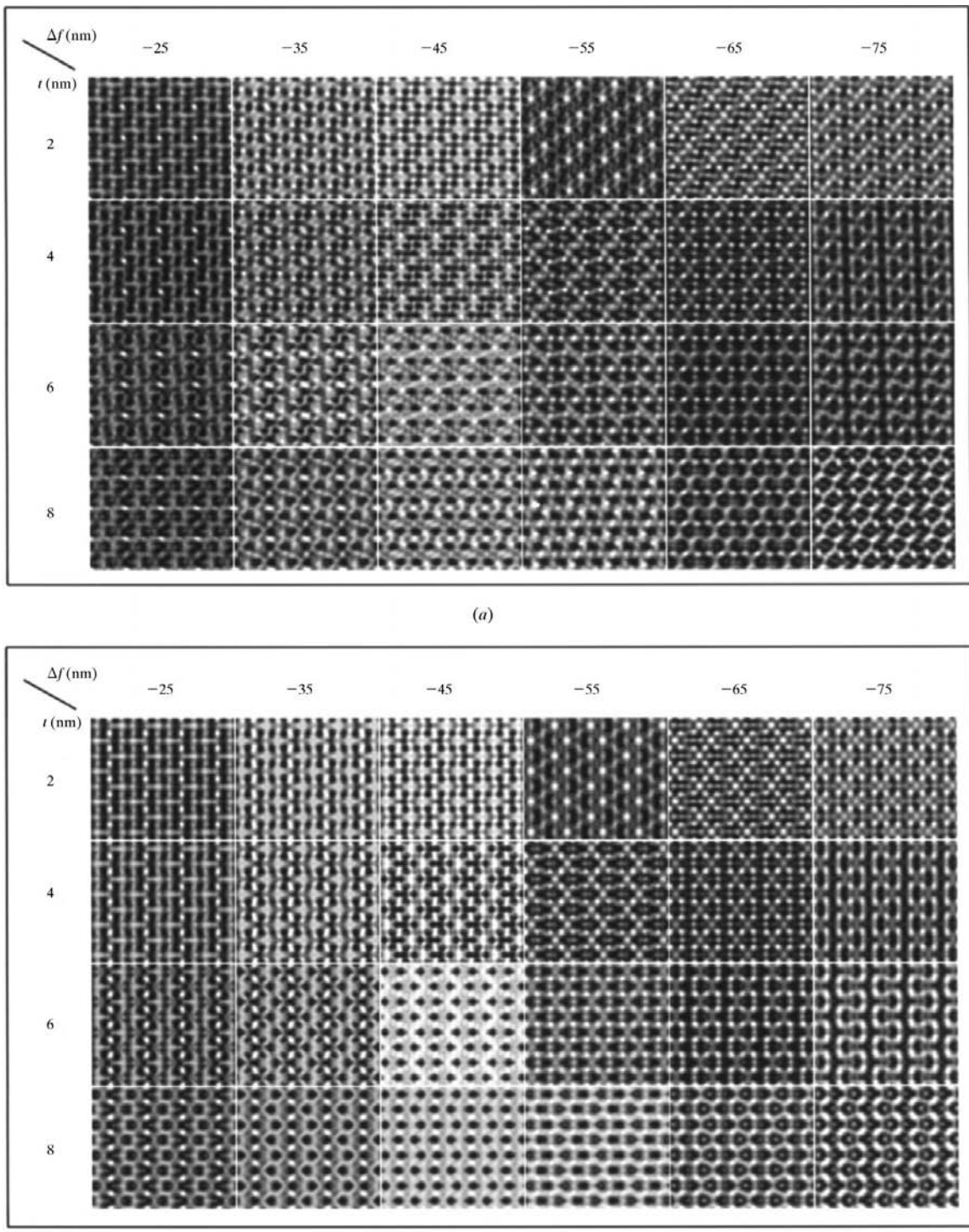

Fig. 8. Calculated HREM images for the $[010]_m$ zone of β-$Ba_3DyAl_2O_{7.5}$ (*a*) and for the $[100]_o$ zone of α-$Ba_3DyAl_2O_{7.5}$ (*b*) for different thicknesses and defocus values.

spot rows that are roughly perpendicular to the unsplit row is ~2.5°, which is consistent with the monoclinic angle $\beta = 91.298\ (9)^\circ$ as determined by X-ray diffraction. A model viewed along the $[010]_m$ zone (Fig. 10) is in accordance with the observed image contrast (Fig. 9). Note that the best coherence of the twinned structures is achieved after a lateral shift of the structures over $1/2a_m$ parallel to the interface. Along the habit plane, a slab consisting of DyO_6 octahedra and AlO_4 tetrahedra exhibiting a glide mirror plane ensures the contact. The space-group considerations mentioned above are consistent with the loss of a glide mirror plane in the space group of the α phase on going through the $\alpha \leftrightarrow \beta$ transition. This glide mirror plane is perpendicular to $b_o = c_m$ and becomes the coherent twin plane of the monoclinic β structure. Since only one mirror plane is lost due to the decrease of point-group symmetry from $2mm$ (α phase) to m (β phase), all twin interfaces are parallel.

The presence of structural oxygen vacancies confined to the strings of vertex-sharing tetrahedra pairs is an important feature of the structure and we will show that it plays a key role in the phase-transition process.

We note that two different twin-related string configurations result when the oxygen vacancies are located at different positions in the string. This is shown schematically in Fig. 11. Transformation of one configuration into the other one can be achieved by a progressive short-range migration of the vacancies along the string following the solid line path in Fig. 11. In the orthorhombic phase, *i.e.* above the transition temperature, the distribution of vacancies along the string is presumably close to random and hence also the tetrahedra pairs are randomly distributed over the two orientations. Under these conditions, the configuration in the string is probably continuously changing in time as a result of the thermal migration of the vacancies. One defined string configuration is only stabilized when the positions of the oxygen vacancies are fixed. Thereby, the vacancies tend to become equally spaced (*i.e.* ordered) because of their mutual repulsion. Since the vacancies can order in two distinct energetically equivalent configurations (Fig. 11), two different structures arise. It is hereby assumed that due to elastic interactions the deformations in neighboring strings will tend to become similar and furthermore impose or at least bias the deformation pattern of the rest of the oxygen framework in which oxygen diffusion is much more difficult owing to the absence of structural vacancies.

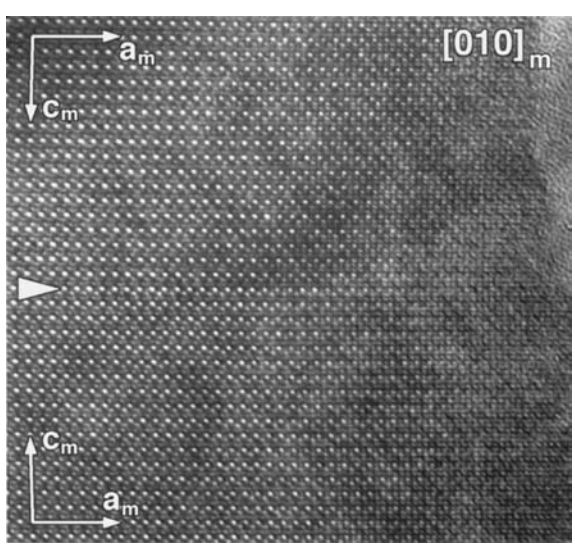

Fig. 9. HREM image of a twin interface between $[010]_m$- and $[0\bar{1}0]_m$-oriented parts of β-$Ba_3DyAl_2O_{7.5}$. The twin boundary is marked by an arrow.

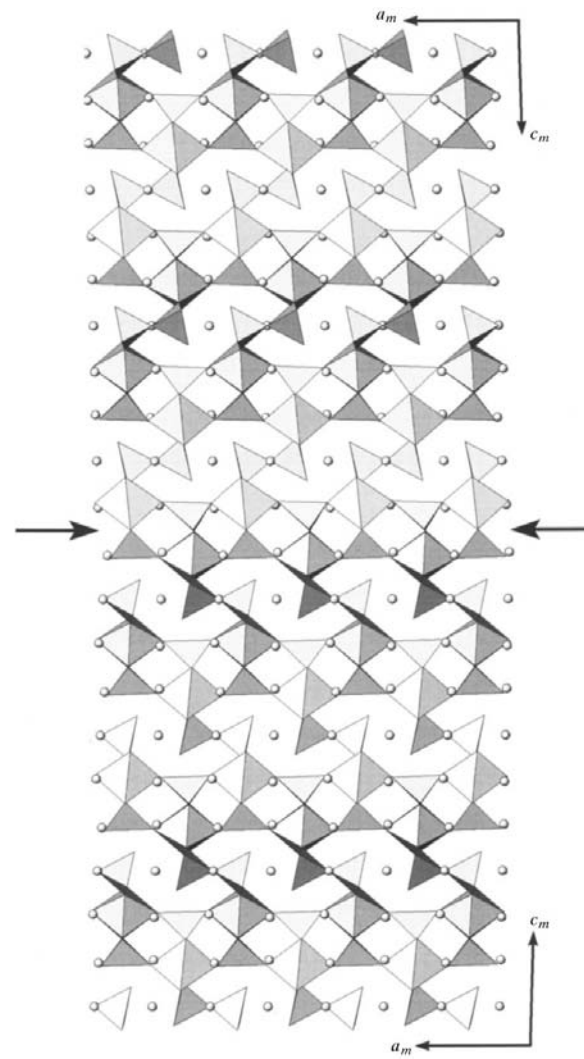

Fig. 10. Structural model of the twin interface which is in agreement with the HREM image in Fig. 9. The glide mirror plane connecting the twinned parts is marked by arrows.

On transformation, the *C*-centered orthorhombic unit cell becomes a slightly deformed primitive monoclinic unit cell with roughly the same cell dimensions. This means that the symmetry translations of the type $1/2[110]_o$ are lost in the transition. Such vectors become potential translation vectors of translation domain interfaces leading to antiphase boundary formation. In the $[100]_m$ high-resolution image (Fig. 12), the separation of the brightest dot rows is 18.4 Å corresponding to the repeat distance $c_m = b_o$. However, as indicated in Fig. 12 by bars, a singular line spacing of 9.2 Å separates two regions exhibiting the normal 18.4 Å spacing. This spacing singularity marks an interface with a displacement vector $1/2[110]_o = 1/2[011]_m$. This displacement leads to a relative shift of the two parts over $1/2b_m$ along a direction parallel to the interface plane.

Owing to the highly preferential migration of vacancies along the strings, it can be rationalized that domains will be limited by planes formed by such strings, *i.e.* by $(001)_m$ planes. The growth of one twin domain at the expense of the adjacent one can then proceed by the progressive migration of vacancies along the strings in the contact plane. In the process, a string may consist in part of pairs of tetrahedra in one orientation and for another part of pairs of tetrahedra in the other orientation. The effective width of a twin band is hereby locally changed, *i.e.* exhibiting a 'ledge'. The lateral displacement of the twin interface is thus a consequence of the migrations of such a ledge.

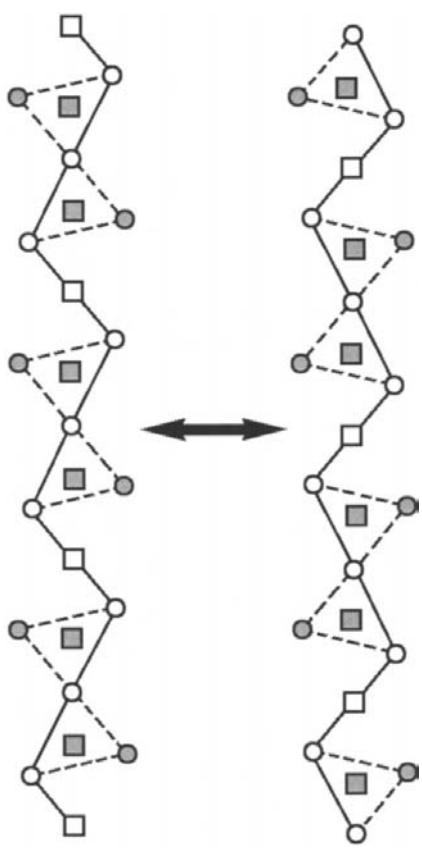

Fig. 11. Schematic representation of two distinct orientations of Al–O strings. The shaded circles mark the O atoms that connect DyO_6 octahedra and AlO_4 tetrahedra. O atoms taking part in the diffusion process are shown as open circles. The displacement path is outlined by the solid line. Structural O vacancies and Al cations are shown as open and shaded squares, respectively.

4. Conclusions

The $Ba_3RM_2O_{7.5}$ complex oxides (R = rare-earth elements, M = Al, Ga) were characterized by a combination of X-ray diffraction and electron microscopy. The monoclinic $Ba_3RGa_2O_{7.5}$, the low-temperature monoclinic β-$Ba_3RAl_2O_{7.5}$ and the high-temperature orthorhombic α-$Ba_3RAl_2O_{7.5}$ can be considered as anion-deficient perovskites with an ordering of R and M cations on the B positions. The high-temperature X-ray diffraction and the DTA study reveal the reversible $\beta \leftrightarrow \alpha$ phase transition with a critical temperature decreasing linearly with the rare-earth-element size. This order–disorder phase transformation results from a sequential displacement of O atoms along the strings of vertex-sharing tetrahedral Al_2O_7 pairs leading to either an ordered occupation of the O-atom positions within the strings (β phase) or a disordered distribution of O atoms over the two possible anion positions (α phase). *In situ* ED and HREM observations of the phase transition revealed a decreasing symmetry from $Cmc2_1$ (α

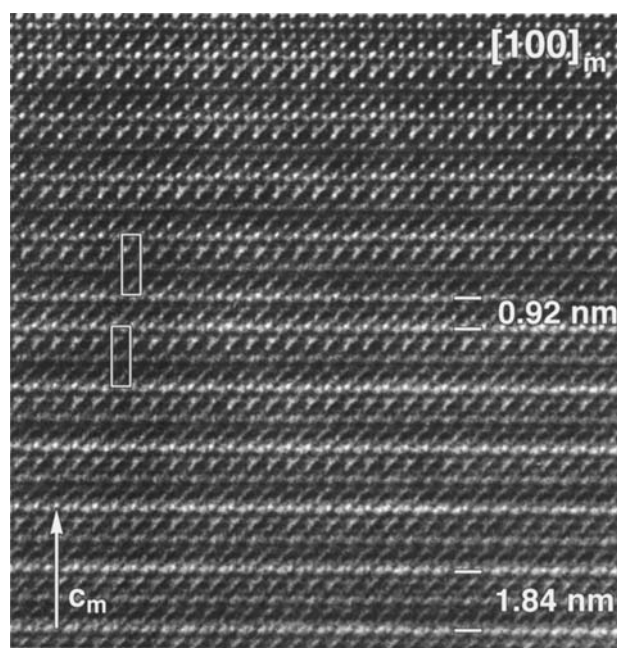

Fig. 12. $[100]_m$ HREM image showing an antiphase boundary. The presence of the interface can be deduced from the 9.2 Å spacing between the brightest rows. The unit cells on both sides of the interface are outlined.

phase) to *Pc* (β phase). The decrease in point symmetry and the loss of translation symmetry lead to the formation of numerous twins and antiphase boundaries in the microstructure of the β phase.

This work was supported by the Russian Science Foundation (grant No. 97-03-33432a). AMA and OIL are grateful to DWTC and FWO (Belgium), respectively, for financial support during their stay at the University of Antwerp. This work has been performed within the framework of IUAP 4/10.

References

Akselrud, L. G., Grin, Yu. N., Zavalij, P. Yu., Pecharsky, V. K. & Fundamentsky, V. S. (1989). 12th European Crystallographic Meeting, Moscow, USSR, Abstracts, p. 155.

Izumi, F. (1993). *The Rietveld Method*, edited by R. A. Young, ch. 13. Oxford University Press.

Kovba, L. M., Lykova, L. N., Antipov, E. V. & Rozova, M. G. (1984). *Zh. Neorg. Khim.* **29**, 3137–3142.

Kovba, L. M., Lykova, L. N. & Rozova, M.G. (1987). *Zh. Neorg. Khim.* **32**, 2011–2013.

Mevs, H. & Müller-Bushbaum, H. (1990). *J. Less-Common. Met.* **158**, 147–152.

Porotnikov, N. V., Antipov, E. V., Lykova, L. N., Kovba, L. M. & Shpanchenko, R. V. (1991). *Zh. Neorg. Khim.* **36**, 1804–1809.

Rüter, I. & Müller-Bushbaum, H. (1989*a*). *Monatsh. Chem.* **120**, 1069–1074.

Rüter, I. & Müller-Bushbaum, H. (1989*b*). *Z. Anorg. Allg. Chem.* **573**, 89–94.

Rüter, I. & Müller-Bushbaum, H. (1990*a*). *J. Less-Common Met.* **162**, 175–180.

Rüter, I. & Müller-Bushbaum, H. (1990*b*). *Z. Anorg. Allg. Chem.* **585**, 82–86.

Rüter, I. & Müller-Bushbaum, H. (1990*c*). *Z. Anorg. Allg. Chem.* **588**, 97–101.